

An efficient model reduction method for solving viscous G-equations in incompressible cellular flows

Haotian Gu^a, Jack Xin^b, Zhiwen Zhang^{c,*}

^a*Department of Mathematics, University of California at Berkeley, Berkeley, CA 94720, USA.*

^b*Department of Mathematics, University of California at Irvine, Irvine, CA 92697, USA.*

^c*Department of Mathematics, The University of Hong Kong, Pokfulam Road, Hong Kong SAR.*

Abstract

The G-equation is a well-known model for studying front propagation in turbulent combustion. In this paper, we shall develop an efficient model reduction method for solving viscous G-equations in incompressible steady and time periodic cellular flows. Our method is based on the Galerkin proper orthogonal decomposition (POD) methods. To facilitate the algorithm design and convergence analysis, we decompose the solution of the viscous G-equation into a mean-free part and a mean part, where their evolution equations can be derived accordingly. We construct the POD basis from the solution snapshots of the mean-free part. With the POD basis, we can efficiently solve the evolution equation for the mean-free part of the solution to the viscous G-equation. After we get the mean-free part of the solution, the mean of the solution can be recovered. We also provide rigorous convergence analysis for our numerical method. Numerical results are presented to demonstrate the accuracy and efficiency of the proposed method. Specifically, we study the turbulent flame speeds of the viscous G-equations in incompressible cellular flows based on the POD method and fully resolved computations.

AMS subject classification: 65M12, 70H20, 76F25, 78M34, 80A25.

Keywords: Viscous G-equation; Hamilton-Jacobi equation; front speed computation; cellular flows; proper orthogonal decomposition (POD); error estimates.

1. Introduction

Front propagation in turbulent combustion is a nonlinear and complicated dynamical process. The G-equation has been a very popular field model in combustion and physics literature for studying premixed turbulent flame propagation [8, 9, 3, 12, 10, 16]. The G-equation model is a sound phenomenological approach to study turbulent combustion, which uses the level-set formulation to study the flame front motion laws with the front

*Corresponding author

Email addresses: htgu@math.berkeley.edu (Haotian Gu), jxin@math.uci.edu (Jack Xin), zhangzw@hku.hk (Zhiwen Zhang)

width ignored. The simplest motion law is that the normal velocity of the front is equal to a constant S_l (the laminar speed) plus the projection of fluid velocity $V(\mathbf{x}, t)$ along the normal. This gives the inviscid G-equation

$$G_t + \mathbf{V} \cdot \nabla G + S_l |\nabla G| = 0 \quad (1)$$

where the set $\{(\mathbf{x}, t) : G(\mathbf{x}, t) = 0\}$ corresponds to the location of the flame front at time t . As fluid turbulence is known to cause stretching and corrugation of flames, additional modeling terms may be incorporated into the basic G-equation. If the curvature term is added into the basic equation to model the curvature effects and the curvature term is further linearized, then we will arrive at the viscous G-equation

$$G_t + \mathbf{V} \cdot \nabla G + S_l |\nabla G| = dS_l \Delta G \quad (2)$$

In order to get numerical solutions of Eq.(2), Liu, Xin and Yu in [7] first approximated the G-equations by a monotone discrete system, then applied high resolution numerical methods such as WENO (weighted essentially non-oscillatory finite difference methods) [5] with a combination of explicit and semi-implicit time stepping strategies, depending on the size and property of dissipation in the equations. However, these existing numerical methods become expensive when we need to solve Eq.(2) many times with different parameters. This motivates us to explore the low-dimension structures of the viscous G-equation (2) and develop efficient model reduction methods to solve them.

One of the most successful model reduction ideas in the study of turbulent flows has been the proper orthogonal decomposition (POD) method. The POD method uses the data from an accurate numerical simulation and extracts the most energetic modes in the system by using the singular value decomposition. This approach may generate low-dimensional structures that play an important role in the dynamics of the flow. The Galerkin POD method has been used to solve many types of partial differential equations, including linear parabolic equations and Burgers equations; see [2, 15] and references therein for details. The interested reader is referred to [1] for a comprehensive introduction of the model reduction methods.

In this paper, we shall study the POD method to solve the viscous G-equation (2). To deal with the periodic boundary condition of the problem, we decompose the solution of the viscous G-equation into a mean-free part and a mean part, where their evolution equations can be derived accordingly. We construct the POD basis from the solution snapshots of the mean-free part since the mean of the solution can be recovered from the mean-free part. The POD basis can be used to compute long-time solution of the viscous G-equation or the viscous G-equations with different parameters. We provide rigorous convergence analysis and show that the accuracy of our method is guaranteed. Finally, we conduct numerical experiments to demonstrate the accuracy and efficiency of the proposed method. In particular, we numerically study the turbulent flame speeds of the viscous G-equations in incompressible steady and time periodic cellular flows, which has many important applications in the turbulent combustion. We remark that our POD

method can be easily extended to solve other types of G-equations [7]. To the best of our knowledge, our study is the first one on POD method to solve G-equations.

The rest of this paper will be organized as follows. In Section 2, we shall give a brief derivation of G-equation models. In Section 3, we show the detailed derivations of the model reduction method for G-equations. In Section 4, we provide the convergence analysis of the proposed method for G-equations. Our proof is based on the backward Euler-Galerkin-POD approximation scheme. However, the proofs for other discretization schemes can be obtained in a similar manner. In Section 5, we shall perform numerical experiments to test the performance and accuracy of the proposed method. We find that POD method can provide considerable savings over existing numerical methods in solving the G-equation while its numerical error is relatively small. Finally, the concluding remarks will be given in Section 6. In the two appendices, we provide the derivation of a finite difference scheme in solving G-equation proposed in [7] and the procedure of the POD method in constructing basis.

2. Turbulent combustion and G-equations

2.1. Derivation of the G-equations

In this section, we briefly introduce the derivation of the G-equation in turbulent combustion. In a thin reaction zone regime and the corrugated flamelet regime of premixed turbulent combustion (Chapter 2 of [12]), the flame front is modeled by a level set function: $\{(x, t) : G(x, t) = 0, x \in R^n\}$, which is the interface between the burned area, denoted by $\{G < 0\}$ and the unburned area, denoted by $\{G > 0\}$, respectively. Therefore, one can study the propagation of the flame front by solving the dynamic equation for the level set function, namely the G-equation. The simplest motion law for the particles on

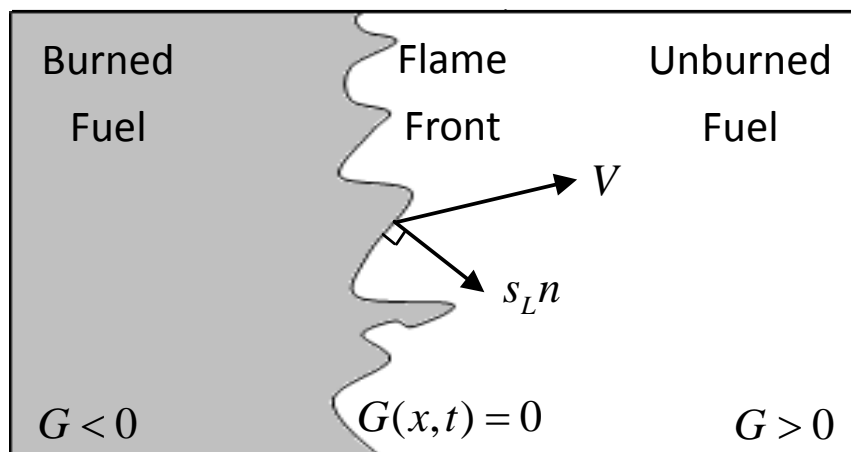


Figure 1: Illustration of local interface velocities in the G-equation and a flame front in a 2D space

the interface is that the normal velocity of the interface is the sum of a constant S_L and

the projection of fluid velocity $\mathbf{V}(x, t)$ along the normal direction (see Fig.1). Hence, the trajectory of a particle $\mathbf{x}(t)$ on the interface satisfies,

$$\frac{d\mathbf{x}}{dt} = \mathbf{V}(\mathbf{x}, t) + S_l \mathbf{n} \quad (3)$$

where S_l is the laminar flame speed and \mathbf{n} is the normal vector. In terms of the level set function, the motion law (3) gives the inviscid G-equation,

$$G_t + \mathbf{V} \cdot \nabla G + S_l |\nabla G| = 0 \quad (4)$$

where ∇ denotes the gradient operator. Thus, the normal vector in (3) can be computed using $\mathbf{n} = \nabla G / |\nabla G|$. Notice that the set $\{G(\mathbf{x}, t) = 0\}$ corresponds to the location of the flame front at time t .

To take into account the effect of flame stretching and corrugation, additional modeling terms may be added into the inviscid G-equation (4). Then, one can obtain extended G-equation models involving curvature effects. The curvature G-equation is

$$G_t + \mathbf{V} \cdot \nabla G + S_l |\nabla G| = d S_l |\nabla G| \left(\nabla \cdot \frac{\nabla G}{|\nabla G|} \right), \quad (5)$$

where d is called the Markstein number. The curvature dependent motion is well-known; see [11, 10] and references therein. If the curvature term is linearized, we obtain the viscous G-equation as follows, which is the research focus here.

$$G_t + \mathbf{V} \cdot \nabla G + S_l |\nabla G| = d S_l \Delta G. \quad (6)$$

2.2. A periodic initial value problem

Now given a unit vector $\mathbf{P} \in \mathbb{R}^n$, where n is the dimension of the physical space, we shall consider the viscous G-equation (6) with planar initial condition

$$\begin{cases} G_t + \mathbf{V} \cdot \nabla G + S_l |\nabla G| = d S_l \Delta G & \text{in } \mathbb{R}^n \times (0, \infty), \\ G(\mathbf{x}, 0) = \mathbf{P} \cdot \mathbf{x} & \text{on } \mathbb{R}^n \times \{t = 0\}. \end{cases} \quad (7)$$

Here, we assume the flame front propagates in direction \mathbf{P} with the initial front being $\{\mathbf{P} \cdot \mathbf{x} = 0\}$ and $\mathbf{x} = (x_1, x_2, \dots, x_n)$. In this paper, we assume $V(\mathbf{x}, t)$ is spatially periodic with C^1 in \mathbf{x} and C^0 in t . Moreover, $V(\mathbf{x}, t)$ is divergence-free (i.e., $\nabla_{\mathbf{x}} \cdot V(\mathbf{x}, t) = 0, \forall t$) and uniformly bounded (i.e., $\|V(\mathbf{x}, t)\|_{\infty} \leq A$).

If we write $G(\mathbf{x}, t) = \mathbf{P} \cdot \mathbf{x} + u(\mathbf{x}, t)$, then $u(\mathbf{x}, t)$ is also spatially periodic and satisfies the following periodic initial value problem

$$\begin{cases} u_t + \mathbf{V} \cdot (\mathbf{P} + \nabla u) + S_l |\mathbf{P} + \nabla u| = d S_l \Delta u & \text{in } \mathbb{T}^n \times (0, \infty), \\ u(\mathbf{x}, 0) = 0 & \text{on } \mathbb{T}^n \times \{t = 0\}, \end{cases} \quad (8)$$

where $\mathbb{T}^n = [0, 1]^n$. Hence we can reduce the numerical computation of Eq.(7) on the whole domain to Eq.(8) on $[0, 1]^n$ by imposing the affine periodic condition:

$$\begin{cases} G_t + \mathbf{V} \cdot \nabla G + S_l |\nabla G| = dS_l \Delta G & \text{in } \mathbb{T}^n \times (0, \infty) \\ G(\mathbf{x}, 0) = \mathbf{P} \cdot \mathbf{x} & \text{on } \mathbb{T}^n \times \{t = 0\} \end{cases} \quad (9)$$

with the assumption $G(\mathbf{x} + \mathbf{z}, t) = G(\mathbf{x}, t) + \mathbf{P} \cdot \mathbf{z}$.

To illustrate the main idea of our method, we choose $\mathbf{P} = \mathbf{e}_1 = (1, 0, \dots, 0)$ and have $G(\mathbf{x}, t) = x_1 + u(\mathbf{x}, t)$. Let $\mathcal{A}(t)$ denote the volume of the burned area that has invaded during time interval $(0, t)$. Then, the turbulent flame speed S_T is defined as the linear growth rate of $\mathcal{A}(t)$. Notice that $G(\mathbf{x}, 0) = x_1$ and $G(\mathbf{x} + \mathbf{e}_1, t) = G(\mathbf{x}, t) + 1$. Then, the S_T can be evaluated by $G(\mathbf{x}, t)$ or $u(\mathbf{x}, t)$ in $[0, 1]^n$,

$$S_T = \lim_{t \rightarrow \infty} \frac{-1}{t} \int_{[0,1]^n} G(\mathbf{x}, t) d\mathbf{x} = \lim_{t \rightarrow \infty} \frac{-1}{t} \int_{[0,1]^n} (x_1 + u(\mathbf{x}, t)) d\mathbf{x} \quad (10)$$

There are many numerical methods to solve the viscous G-equation (9) or Eq.(8) on a bounded physical domain \mathbb{T}^n . For instance, we can employ the Hamilton-Jacobi weighted essentially non-oscillatory (HJ-WENO) scheme and the total variation diminishing Runge-Kutta (TVD-RK) scheme in higher order spatial and time discretization respectively. See [13, 5, 10, 7] for details of the schemes. To make our paper self-contained, we show the numerical schemes proposed by the second author in the appendix 7.1; see [7] for more details.

3. Model reduction method for G-equations

In practice, we are interested in studying the dependence of the turbulent flame speed S_T on different parameters in the viscous G-equation, such as the Markstein number d . As such, we have to solve the viscous G-equation many times, which is an expensive task. Therefore, we need to design numerical methods that allow us to efficiently and accurately solve the viscous G-equation. We shall develop an efficient model reduction method to achieve this goal.

3.1. A decomposition strategy

According to the definition in (10), we can either solve Eq.(8) to obtain $u(x, t)$ or solve Eq.(9) to obtain $G(x, t)$, in order to compute the turbulent flame speed S_T . We shall consider to solve Eq.(8) since it is easier to deal with the boundary condition. Let us decompose the solution u of Eq.(8) into $\hat{u} + \bar{u}$, where \hat{u} is the mean-free part and \bar{u} is the mean of u . This decomposition means that

$$\int_{\mathbb{T}^n} \hat{u}(\mathbf{x}, t) d\mathbf{x} = 0, \quad \forall t \quad \text{and} \quad \bar{u}(t) = \int_{\mathbb{T}^n} u(\mathbf{x}, t) d\mathbf{x}. \quad (11)$$

Then, substituting $u = \hat{u} + \bar{u}$ into (8), we obtain

$$\hat{u}_t + \bar{u}_t + \mathbf{V} \cdot (\mathbf{P} + \nabla \hat{u}) + S_l |\mathbf{P} + \nabla \hat{u}| - dS_l \Delta \hat{u} = 0. \quad (12)$$

Integrating the above equation over the domain \mathbb{T}^n gives

$$\int_{\mathbb{T}^n} [\hat{u}_t + \bar{u}_t + \mathbf{V} \cdot (\mathbf{P} + \nabla \hat{u}) - dS_l \Delta \hat{u}] d\mathbf{x} = - \int_{\mathbb{T}^n} S_l |\mathbf{P} + \nabla \hat{u}| d\mathbf{x}. \quad (13)$$

The definitions of \bar{u} and \hat{u} in (11) imply that $\int_{\mathbb{T}^n} \hat{u}_t = 0$ and $\int_{\mathbb{T}^n} \bar{u}_t = \bar{u}_t$. Furthermore, the periodic conditions of \mathbf{V} and \hat{u} imply $\int_{\mathbb{T}^n} \mathbf{V} \cdot \mathbf{P} = 0$, $\int_{\mathbb{T}^n} \Delta \hat{u} = 0$, and $\int_{\mathbb{T}^n} \mathbf{V} \cdot \nabla \hat{u} = 0$, where we have used the facts that \mathbf{V} is divergence-free and \hat{u} is the mean-free. Combining these results, we can simplify the Eq.(13) as,

$$\bar{u}_t = - \int_{\mathbb{T}^n} S_l |\mathbf{P} + \nabla \hat{u}| d\mathbf{x}. \quad (14)$$

Finally, we find that the Eq.(8) is equivalent to

$$\begin{cases} \hat{u}_t + \mathbf{V} \cdot \nabla \hat{u} - dS_l \Delta \hat{u} + S_l |\mathbf{P} + \nabla \hat{u}| - \int_{\mathbb{T}^n} S_l |\mathbf{P} + \nabla \hat{u}| d\mathbf{x} + \mathbf{V} \cdot \mathbf{P} = 0 & \text{in } \mathbb{T}^n \times (0, \infty) \\ \bar{u}_t = - \int_{\mathbb{T}^n} S_l |\mathbf{P} + \nabla \hat{u}(\mathbf{x}, t)| d\mathbf{x} & \text{on } t \in (0, \infty) \\ \hat{u}(\mathbf{x}, 0) = 0 & \text{on } \mathbb{T}^n \times \{t = 0\} \\ \bar{u}(0) = 0 & \end{cases} \quad (15)$$

The strategy of decomposing the solution u into \hat{u} and \bar{u} plays a crucial role in the convergence analysis of our model reduction method.

3.2. Construction of the POD basis

In this section, we shall present our model reduction method to solve Eq.(15). Since the evolution equation for \bar{u} depends on \hat{u} , we first consider to solve the equation for \hat{u} , i.e.,

$$\hat{u}_t + \mathbf{V} \cdot \nabla \hat{u} - dS_l \Delta \hat{u} + S_l |\mathbf{P} + \nabla \hat{u}| - \int_{\mathbb{T}^n} S_l |\mathbf{P} + \nabla \hat{u}| d\mathbf{x} + \mathbf{V} \cdot \mathbf{P} = 0, \text{ in } \mathbb{T}^n \times (0, \infty). \quad (16)$$

Let $H_{per}^1(\mathbb{T}^n)$ denote the Sobolev space on the domain \mathbb{T}^n with a periodic boundary condition, and let $\langle \cdot, \cdot \rangle$ denote the standard inner product on $L^2(\mathbb{T}^n)$. Let $H \subset H_{per}^1(\mathbb{T}^n)$ be the subspace consisting of all mean-free functions. Since H is a closed subspace of $H_{per}^1(\mathbb{T}^n)$, H itself is a Hilbert space. Let $\langle \cdot, \cdot \rangle_H$ denote the standard inner product on H . Define the bilinear form $a(\cdot, \cdot) : H \times H \rightarrow \mathbb{R}$ to be

$$a(u, v) = \int_{\mathbb{T}^n} [(\mathbf{V} \cdot \nabla u)v + dS_l(\nabla u \cdot \nabla v)] d\mathbf{x}. \quad (17)$$

Also, define a nonlinear map from H to $L^2(\mathbb{T}^n)$ to be

$$F(u) = S_l |\mathbf{P} + \nabla u| - \int_{\mathbb{T}^n} S_l |\mathbf{P} + \nabla u| d\mathbf{x}. \quad (18)$$

The weak formulation of (16) is

$$\langle \hat{u}_t, \psi \rangle + a(\hat{u}, \psi) + \langle F(u), \psi \rangle = \langle -\mathbf{P} \cdot \mathbf{V}, \psi \rangle, \quad \forall \psi \in H, \quad (19)$$

which can be solved using numerical methods, such as the finite element method.

Assume we have obtained a set of numerical solutions $\{\hat{u}(\cdot, t_k)\}$ to Eq.(16), where $t_k = k\Delta t$, $\Delta t = T/m$, $k = 0, \dots, m$. Then, we use $2m + 1$ snapshots $\{\hat{u}(\cdot, t_0), \dots, \hat{u}(\cdot, t_m), \bar{\partial}\hat{u}(\cdot, t_1), \dots, \bar{\partial}\hat{u}(\cdot, t_m)\}$, where $\bar{\partial}\hat{u}(t_i) = (\hat{u}(t_i) - \hat{u}(t_{i-1}))/\Delta t$, to generate the POD basis functions. By adding the terms $\bar{\partial}\hat{u}(t_i)$, $i = 1, \dots, m$ into the snapshots, we can obtain more accurate POD basis functions and avoid an extra $(\Delta t)^{-2}$ factor in the convergence analysis; see Section 4 for more details.

Let $S^r = \{\psi_1(\cdot), \psi_2(\cdot), \dots, \psi_r(\cdot)\}$ denote the r -dimensional POD basis functions obtained from the $2m + 1$ snapshots, which minimize the following error

$$\frac{1}{2m+1} \sum_{i=0}^m \|\hat{u}(t_i) - \sum_{j=1}^r \langle \hat{u}(t_i), \psi_j \rangle_H \psi_j\|_H^2 + \frac{1}{2m+1} \sum_{i=0}^m \|\bar{\partial}\hat{u}(t_i) - \sum_{j=1}^r \langle \bar{\partial}\hat{u}(t_i), \psi_j \rangle_H \psi_j\|_H^2. \quad (20)$$

Remark 3.1. In practice, we can use experimental data or reference numerical methods to generate solution snapshots. Moreover, we can compute a set of numerical solutions $\{G(\cdot, t)\}$ to Eq.(9) and extract the mean-free parts to obtain our solution snapshots.

Remark 3.2. The construction of the POD basis can be costly. However, once the construction is done, POD basis can be used to solve the viscous G-equations with different parameters, which will bring significant computational savings.

3.3. A backward Euler and POD-based Galerkin method

The POD basis provides an efficient approach to approximate the solution in the physical space. If we choose the backward Euler scheme to discretize the time space, we obtain a backward Euler and POD-based Galerkin method to solve Eq.(16). Specifically, let $\hat{U}_k \equiv \sum_{i=1}^r a_i(t_k) \psi_i$ denote the numerical solution at $t = t_k$, where ψ_i 's are the POD basis functions. We want to find solutions $\{\hat{U}_k\}_{k=0}^m \subset S^r$ satisfying

$$\begin{cases} \langle \bar{\partial}\hat{U}_k, \psi \rangle + a(\hat{U}_k, \psi) + \langle F(\hat{U}_k), \psi \rangle = \langle -\mathbf{P} \cdot \mathbf{V}, \psi \rangle, & \forall \psi \in S^r \\ \hat{U}_0(\mathbf{x}) = 0, \end{cases} \quad (21)$$

where $\bar{\partial}\hat{U}_k = (\hat{U}_k - \hat{U}_{k-1})/\Delta t$. By choosing the test function ψ to be ψ_i , $i = 1, \dots, r$ in (21) and letting $A_k = (a_1(t_k), \dots, a_r(t_k))^T$ denote the coefficient vector, we obtain a nonlinear equation system for A_k as

$$M_1 A_k = M_2 A_{k-1} + C + F_k, \quad (22)$$

where $M_1, M_2 \in \mathbb{R}^{r \times r}$ with $(M_1)_{ij} = \langle \psi_i, \psi_j \rangle + \Delta t \cdot a(\psi_i, \psi_j)$ and $(M_2)_{ij} = \langle \psi_i, \psi_j \rangle$, and $C, F_k \in \mathbb{R}^r$ with $C_i = -\Delta t \langle \mathbf{V} \cdot \mathbf{P}, \psi_i \rangle$ and $(F_k)_i = -\Delta t \langle F(\sum_{i=1}^r a_i(t_k) \psi_i), \psi_i \rangle$. The matrices M_1, M_2 and C can be pre-computed and saved. The Eq.(22) can be efficiently computed

using the Newton's method, where the solution at time t_{k-1} can be chosen as the initial guess for A_k .

We solve Eq.(22) to get the POD solution \hat{U}_k , which is the numerical solution of the mean-free part $\hat{u}(\mathbf{x}, t)$ of the G-equation (16). As indicated by the Eq.(15), $u(\mathbf{x}, t)$ is recovered by add the mean solution back

$$u(\mathbf{x}, t) = \hat{u}(\mathbf{x}, t) - \int_0^t \int_{\mathbb{T}^n} S_l |\mathbf{P} + \nabla \hat{u}(\mathbf{x}, t)| dx dt.$$

Therefore, the numerical solution to $u(\mathbf{x}, t)$ is

$$U_k = \hat{U}_k - \Delta t \sum_{i=1}^k \left[\int_{\mathbb{T}^n} S_l |\mathbf{P} + \nabla \hat{U}_i(\mathbf{x}, t)| \right]. \quad (23)$$

In practice, we apply a second-order trapezoidal rule to compute the numerical integration in (23). Meanwhile, we use a central difference scheme to compute the spatial derivatives and use extrapolations at boundaries to approximate spatial derivatives to maintain the second order accuracy.

4. Convergence analysis

In this section, we shall present some convergence analysis to show that the accuracy of our numerical solution is guaranteed. Our convergence analysis follows the framework of the Galerkin finite element methods for parabolic problems [14]. To deal with the nonlinearity of the viscous G-equation, the following lemmas are useful.

Lemma 4.1. *There exists a constant $\gamma > 0$ such that for any $u, v \in H$,*

$$\|F(u) - F(v)\|_{L^2} \leq \gamma \|u - v\|_H \quad (24)$$

Proof. The proof of this lemma is based the definition of F (see Eq.(18)) and the triangle inequality. \square

Lemma 4.2. *The bilinear form $a(\cdot, \cdot)$ (defined in (17)) is continuous and coercive, which means that there exist constants $\beta > 0$ and $\kappa > 0$ such that for any $\psi, \phi \in H$*

$$a(\psi, \phi) \leq \beta \|\psi\|_H \|\phi\|_H, \quad a(\psi, \psi) \geq \kappa \|\psi\|_H^2. \quad (25)$$

Proof. Let $\|\mathbf{V}\|_\infty$ denote the maximum amplitude of the vector field \mathbf{V} . One has the estimate

$$\begin{aligned} a(\psi, \phi) &\leq \int_{\mathbb{T}^n} \|\mathbf{V}\|_\infty |\nabla \psi| \cdot |\phi| + d S_l |\nabla \psi| \cdot |\nabla \phi| \\ &\leq \|\mathbf{V}\|_\infty \|\psi\|_H \|\phi\|_H + d S_l \|\psi\|_H \|\phi\|_H. \end{aligned}$$

The last inequality follows from the Cauchy-Schwarz inequality. Moreover, since \mathbf{V} is divergence-free, $\mathbf{V} \cdot \nabla$ is skew-symmetric, which means

$$a(\psi, \psi) = dS_l \int_{\mathbb{T}^n} |\nabla \psi|^2.$$

Since ψ is mean-free, the Poincaré-Wirtinger inequality implies that there exists a constant $\kappa > 0$ such that

$$a(\psi, \psi) \geq \kappa \|\psi\|_H^2.$$

□

Now we define the Ritz-projection $P^r : H \rightarrow S^r$, $u \mapsto P^r u$ such that

$$a(P^r u, \psi) = a(u, \psi), \quad \forall \psi \in S^r. \quad (26)$$

Facts from functional analysis guarantee that P^r is well-defined and bounded because $a(\cdot, \cdot)$ is continuous and coercive. More specifically,

$$\|P^r u\|_H \leq \frac{\beta}{\kappa} \|u\|_H, \quad \forall u \in H. \quad (27)$$

Using the same argument in Lemma 3 and Lemma 4 in [6], we can prove that P^r has the following approximation property. More details of the approximation property of the POD basis can be found in the appendix 7.2.

Lemma 4.3.

$$\frac{1}{m} \sum_{k=1}^m \|\hat{u}(t_k) - P^r \hat{u}(t_k)\|_H^2 \leq \frac{3\beta}{\kappa} \sum_{k=r+1}^m \lambda_k, \quad (28)$$

and

$$\frac{1}{m} \sum_{k=1}^m \|\bar{\partial} \hat{u}(t_k) - P^r \bar{\partial} \hat{u}(t_k)\|_H^2 \leq \frac{3\beta}{\kappa} \sum_{k=r+1}^m \lambda_k, \quad (29)$$

where λ_k is the k -th largest eigenvalues of the correlation matrix K associated with the solution snapshots.

Theorem 4.4. Let \hat{U} and $\{\hat{U}_k\}_{k=0}^m$ be the solutions to Eq.(19) and its backward Euler-POD-based Galerkin approximation, respectively. Then for sufficiently small Δt , there exists a constant $C > 0$ depending on \hat{u} , d , S_l , \mathbf{V} , \mathbf{P} and T but independent of r , Δt , and m such that

$$\frac{1}{m} \sum_{k=1}^m \|\hat{U}_k - \hat{u}(t_k)\|_{L^2}^2 \leq C((\Delta t)^2 + \sum_{j=r+1}^m \lambda_j). \quad (30)$$

Proof. For $k = 0, 1, \dots, m$, define $\vartheta_k = \hat{U}_k - P^r \hat{u}(t_k)$ and $\varrho_k = P^r \hat{u}(t_k) - \hat{u}(t_k)$. Then

$$\frac{1}{m} \sum_{k=1}^m \|\hat{U}_k - \hat{u}(t_k)\|_{L^2}^2 \leq \frac{2}{m} \sum_{k=1}^m \|\vartheta_k\|_{L^2}^2 + \frac{2}{m} \sum_{k=1}^m \|\varrho_k\|_{L^2}^2, \quad (31)$$

$$\frac{2}{m} \sum_{k=1}^m \|\varrho_k\|_{L^2}^2 \leq \frac{2}{m} \sum_{k=1}^m \|\varrho_k\|_H^2 \leq \frac{6\beta}{\kappa} \sum_{k=r+1}^m \lambda_k. \quad (32)$$

Define $\bar{\vartheta}_k = (\vartheta_k - \vartheta_{k-1})/\Delta t$. For all $\psi \in S^r$,

$$\langle \bar{\vartheta}_k, \psi \rangle + a(\vartheta_k, \psi) = \langle v_k, \psi \rangle + \langle F(\hat{u}(t_k)) - F(\hat{U}_k), \psi \rangle, \quad (33)$$

where $v_k = \hat{u}_t(t_k) - P^r \bar{\vartheta}_k \hat{u}(t_k) = \hat{u}_t(t_k) - \bar{\vartheta}_k \hat{u}(t_k) + \bar{\vartheta}_k \hat{u}(t_k) - P^r \bar{\vartheta}_k \hat{u}(t_k)$. Define $\omega_k = \hat{u}_t(t_k) - \bar{\vartheta}_k \hat{u}(t_k)$ and $\eta_k = \bar{\vartheta}_k \hat{u}(t_k) - P^r \bar{\vartheta}_k \hat{u}(t_k)$. Take $\psi = \vartheta_k \in S^r$ in the previous equality and we obtain

$$\frac{1}{\Delta t} (\|\vartheta_k\|_{L^2}^2 - \langle \vartheta_k, \vartheta_{k-1} \rangle) + \kappa \|\vartheta_k\|_{L^2}^2 \leq \|F(\hat{u}(t_k)) - F(\hat{U}_k)\|_{L^2} \|\vartheta_k\|_{L^2} + \|\vartheta_k\|_{L^2} \|v_k\|_{L^2}. \quad (34)$$

By the Lemma 4.1,

$$\begin{aligned} \|F(\hat{u}(t_k)) - F(\hat{U}_k)\|_{L^2} \|\vartheta_k\|_{L^2} &\leq \gamma \|\hat{u}(t_k) - \hat{U}_k\|_H \|\vartheta_k\|_{L^2}, \\ &\leq \gamma (\|\varrho_k\|_H + \|\vartheta_k\|_H) \|\vartheta_k\|_{L^2}. \end{aligned}$$

Since $\vartheta_k \in S^r$, which is a finite dimensional space, the norms defined on S^r are equivalent. This means that there exist some constant $C_1 > 0$ such that

$$\begin{aligned} \|F(\hat{u}(t_k)) - F(\hat{U}_k)\|_{L^2} \|\vartheta_k\|_{L^2} &\leq C_1 (\|\varrho_k\|_H + \|\vartheta_k\|_{L^2}) \|\vartheta_k\|_{L^2}, \\ &\leq \frac{C_1}{2} \|\varrho_k\|_H^2 + \frac{3C_1}{2} \|\vartheta_k\|_{L^2}^2. \end{aligned}$$

Combining these inequalities, we have

$$\|\vartheta_k\|_{L^2}^2 - \langle \vartheta_k, \vartheta_{k-1} \rangle \leq \Delta t (\|\vartheta_k\|_{L^2} \|\vartheta_k\|_{L^2} + \frac{C_1}{2} \|\varrho_k\|_H^2 + \frac{3C_1}{2} \|\vartheta_k\|_{L^2}^2).$$

By using the inequality of arithmetic and geometric means, we obtain

$$(1 - (1 + C_1)\Delta t) \|\vartheta_k\|_{L^2}^2 \leq \|\vartheta_{k-1}\|_{L^2}^2 + \Delta t (\|\vartheta_k\|_{L^2}^2 + 3C_1 \|\varrho_k\|_H^2).$$

For sufficiently small Δt , there exists a constant $C_2 > 0$ such that

$$\|\vartheta_k\|_{L^2}^2 \leq (1 + C_2 \Delta t) \left(\|\vartheta_{k-1}\|_{L^2}^2 + \Delta t (\|\vartheta_k\|_{L^2}^2 + 3C_1 \|\varrho_k\|_H^2) \right). \quad (35)$$

By iteratively using the inequality (35), we have

$$\|\vartheta_k\|_{L^2}^2 \leq e^{C_2 T} \left(\|\vartheta_0\|_{L^2}^2 + \Delta t \sum_{j=1}^k (\|\vartheta_j\|_{L^2}^2 + 3C_1 \|\varrho_j\|_H^2) \right). \quad (36)$$

Note that $\vartheta_0 = 0$ in our case. Therefore, we sum the inequality (36) from $k = 1$ to m and arrive at

$$\begin{aligned} \sum_{k=1}^m \|\vartheta_k\|_{L^2}^2 &\leq e^{C_2 T} \Delta t \sum_{k=1}^m \sum_{j=1}^k (\|v_j\|_{L^2}^2 + 3C_1 \|\varrho_j\|_H^2), \\ &\leq e^{C_2 T} T \sum_{j=1}^m (\|v_j\|_{L^2}^2 + 3C_1 \|\varrho_j\|_H^2), \\ &\leq e^{C_2 T} T \sum_{j=1}^m (2\|\omega_j\|_{L^2}^2 + 2\|\eta_j\|_{L^2}^2 + 3C_1 \|\varrho_j\|_H^2). \end{aligned}$$

Therefore,

$$\begin{aligned} \frac{1}{m} \sum_{k=1}^m \|\hat{U}_k - \hat{u}(t_k)\|_{L^2}^2 &\leq \frac{2}{m} \sum_{k=1}^m \|\vartheta_k\|_{L^2}^2 + \frac{6\beta}{\kappa} \sum_{k=r+1}^m \lambda_k, \\ &\leq \frac{2e^{C_2 T} T}{m} \sum_{j=1}^m (2\|\omega_j\|_{L^2}^2 + 2\|\eta_j\|_{L^2}^2 + 3C_1 \|\varrho_j\|_H^2) + \frac{6\beta}{\kappa} \sum_{k=r+1}^m \lambda_k. \end{aligned}$$

As proved in the Theorem 7 of [6],

$$\sum_{j=1}^m \|\omega_j\|_{L^2}^2 \leq \frac{\Delta t}{3} \int_0^T \|\hat{u}_{tt}(t)\|_{L^2}^2. \quad (37)$$

Together with Lemma 4.3, we obtain

$$\frac{1}{m} \sum_{k=1}^m \|\hat{U}_k - \hat{u}(t_k)\|_{L^2}^2 \leq \left(\frac{4e^{C_2 T}}{3} \int_0^T \|\hat{u}_{tt}(t)\|_H^2 \right) (\Delta t)^2 + C_3 \sum_{k=r+1}^m \lambda_k,$$

where $C_3 = \frac{3\beta}{\kappa} (2e^{C_2 T} T (2 + 3C_1) + 2)$. This completes the proof for Theorem 4.4. \square

Theorem 4.4 provides an error estimate for the mean-free part. Recall that the mean part depends on the mean-free part and the original solution can be recovered afterward. Thus, we can obtain the error estimate for the original solution.

Theorem 4.5. *Let u and $\{U_k\}_{k=0}^m$ be the solutions to Eq.(8) and its numerical approximation Eq.(23) based on backward Euler-Galerkin-POD scheme, respectively. Then for sufficiently small Δt , there exists a constant $C' \geq 0$ depending on \hat{u} , d , S_l , \mathbf{V} , \mathbf{P} and T but independent of r , Δt , and m such that*

$$\frac{1}{m} \sum_{k=1}^m \|U_k - u(t_k)\|_{L^2}^2 \leq C' ((\Delta t)^2 + \sum_{j=r+1}^m \lambda_j). \quad (38)$$

Proof. Let C be the constant appearing in Theorem 4.4, i.e., the Eq.(30). Recall that

$$U_k = \bar{U}_k + \hat{U}_k = -\Delta t \sum_{i=1}^k \left[\int_{\mathbb{T}^n} S_l |\mathbf{P} + \nabla \hat{U}_i(\mathbf{x}, t)| \right] + \hat{U}_k,$$

and

$$u(t_k) = \bar{u}(t_k) + \hat{u}(t_k) = - \int_0^t \int_{\mathbb{T}^n} S_l |\mathbf{P} + \nabla \hat{u}(\mathbf{x}, t)| dx dt + \hat{u}(t_k).$$

We also denote

$$(\bar{U}_k)_t = - \int_{\mathbb{T}^n} S_l |\mathbf{P} + \nabla \hat{U}_i(\mathbf{x}, t)|.$$

Then we obtain

$$\frac{1}{m} \sum_{k=1}^m \|U_k - u(t_k)\|_{L^2}^2 \leq \frac{2}{m} \sum_{k=1}^m \|\hat{U}_k - \hat{u}(t_k)\|_{L^2}^2 + \frac{2}{m} \sum_{k=1}^m \|\bar{u}(t_k) - \bar{U}_k\|_{L^2}^2. \quad (39)$$

From Theorem 4.4, we get an estimate for the first summation on the RHS of the inequality (39). So in order to prove the estimate (38), we only need to show that there exist a constant $C'' > 0$ independent of r , Δt and m such that

$$\frac{1}{m} \sum_{k=1}^m \|\bar{u}(t_k) - \bar{U}_k\|_{L^2}^2 \leq C'' ((\Delta t)^2 + \sum_{j=r+1}^m \lambda_j).$$

As such, we consider the following decomposition

$$\sum_{k=1}^m \|\bar{u}(t_k) - \bar{U}_k\|_{L^2}^2 \leq 2 \sum_{k=1}^m \left\| \bar{u}(t_k) - \sum_{j=1}^k \Delta t (\bar{u}_t(t_j)) \right\|_{L^2}^2 + 2 \sum_{k=1}^m \left\| \sum_{j=1}^k \Delta t (\bar{u}_t(t_j) - (\bar{U}_j)_t) \right\|_{L^2}^2. \quad (40)$$

The first term on the RHS of the inequality (40) is bounded by

$$\begin{aligned} 2 \sum_{k=1}^m \left\| \bar{u}(t_k) - \sum_{j=1}^k \Delta t (\bar{u}_t(t_j)) \right\|_{L^2}^2 &\leq 2(\Delta t)^2 \sum_{k=1}^m \left\| \sum_{j=1}^k \left(\frac{\bar{u}(t_j) - \bar{u}(t_{j-1})}{\Delta t} - \bar{u}_t(t_j) \right) \right\|_{L^2}^2, \\ &\leq 2(\Delta t)^2 \sum_{k=1}^m k \sum_{j=1}^k \left\| \frac{\bar{u}(t_j) - \bar{u}(t_{j-1})}{\Delta t} - \bar{u}_t(t_j) \right\|_{L^2}^2. \end{aligned} \quad (41)$$

Note that the term $\frac{\bar{u}(t_j) - \bar{u}(t_{j-1})}{\Delta t} - \bar{u}_t(t_j)$ in (41) is basically equal to $-\omega_j$, which was defined in the proof of the Theorem 4.4. The only difference is that we replace \hat{u} in the definition

of the ω_j by \bar{u} . Therefore, we can replace \hat{u} in Eq.(37) by \bar{u} and obtain

$$\begin{aligned} 2 \sum_{k=1}^m \left\| \bar{u}(t_k) - \sum_{j=1}^k \Delta t (\bar{u}_t(t_j)) \right\|_{L^2}^2 &\leq 2(\Delta t)^2 \sum_{k=1}^m k \sum_{j=1}^k \left\| \frac{\bar{u}(t_j) - \bar{u}(t_{j-1})}{\Delta t} - \bar{u}_t(t_j) \right\|_{L^2}^2, \\ &\leq 2(\Delta t)^2 \sum_{k=1}^m k \frac{\Delta t}{3} \int_0^T \|\bar{u}_{tt}(t)\|_{L^2}^2 \\ &\leq \frac{2(\Delta t)^3}{3} \sum_{k=1}^m k \int_0^T |\bar{u}_{tt}(t)|^2 \leq \frac{2T^2}{3} \Delta t \int_0^T |\bar{u}_{tt}(t)|^2. \end{aligned}$$

The second term on the RHS of Eq.(40) is bounded by

$$\begin{aligned} 2 \sum_{k=1}^m \left\| \sum_{j=1}^k \Delta t (\bar{u}_t(t_j) - (\bar{U}_k)_t) \right\|_{L^2}^2 &\leq 2(\Delta t)^2 \sum_{k=1}^m k \sum_{j=1}^k \|\bar{u}_t(t_j) - (\bar{U}_j)_t\|_{L^2}^2, \\ &\leq 2(\Delta t)^2 \sum_{k=1}^m k \sum_{j=1}^k \left(\int_{\mathbb{T}^n} |\nabla(\hat{u}(t_j) - \hat{U}_j)| \right)^2, \\ &\leq 2(\Delta t)^2 m^2 \sum_{j=1}^m \left(\int_{\mathbb{T}^n} |\nabla(\hat{u}(t_j) - \hat{U}_j)| \right)^2, \\ &\leq 2T^2 \sum_{j=1}^m \|\hat{u}(t_j) - \hat{U}_j\|_H^2 \leq 2T^2 C_4 \sum_{j=1}^m \|\hat{u}(t_j) - \hat{U}_j\|_{L^2}^2, \end{aligned}$$

where the last inequality follows from the fact that $\hat{u}(t_j) - \hat{U}_j \in S^r$ and that norms are equivalent in a finite dimensional space. Therefore,

$$\frac{1}{m} \sum_{k=1}^m \|\bar{u}(t_k) - \bar{U}_k\|_{L^2}^2 \leq (\Delta t)^2 \frac{2T}{3} \int_0^T |\bar{u}_{tt}(t)| + 2T^2 C_4 \frac{3\beta}{\kappa} \sum_{j=r+1}^m \lambda_j.$$

This completes the proof. \square

5. Numerical Results

We shall perform numerical experiments to test the performance and accuracy of the proposed method. We consider the following viscous G-equation on $[0, 1]^2$ with planar initial condition

$$\begin{cases} G_t + \mathbf{V} \cdot \nabla G + S_l |\nabla G| = d S_l \Delta G & \text{in } [0, 1]^2 \times (0, T), \\ G(\mathbf{x}, 0) = \mathbf{P} \cdot \mathbf{x} & \text{on } [0, 1]^2 \times \{t = 0\}, \end{cases} \quad (42)$$

where $\mathbf{x} = (x, y)$, \mathbf{P} is the flame front propagation direction, and the assumption $G(\mathbf{x} + \mathbf{z}, t) = G(\mathbf{x}, t) + \mathbf{P} \cdot \mathbf{z}$ is used. The setting of the fluid velocity $\mathbf{V}(\mathbf{x})$ is an important issue

in the turbulent combustion modeling. We first consider a typical velocity field, which is a steady incompressible cellular flow,

$$\mathbf{V}(\mathbf{x}) = (V_1, V_2) = \nabla^\perp \mathcal{H} = (-\mathcal{H}_y, \mathcal{H}_x), \quad \mathcal{H} = \frac{A}{2\pi} \sin(2\pi x) \sin(2\pi y), \quad (43)$$

where A is the amplitude of the velocity field. In our numerical experiments, we choose $A = 4.0$, $S_l = 1$, and $\mathbf{P} = (1, 0)$. In our comparison, the finite difference solution refers to the solution obtained by the reference numerical scheme to solve (42); see Section 7.1 in the appendix for more details. While the POD solution refers to the one obtained by our method, i.e., the solution is represented by the POD basis. We choose the method of snapshot to construct the POD basis; see Section 3.2 for the details.

5.1. Test of the POD basis within the same computational time

In the first numerical experiment, we solve the viscous G-equation (42) from time $t = 0$ to T using the reference numerical scheme and obtain solution snapshots. Then, we construct POD basis function the solution snapshots. Finally, we recompute the viscous G-equation (42) on the same time period $[0, T]$ using the POD basis.

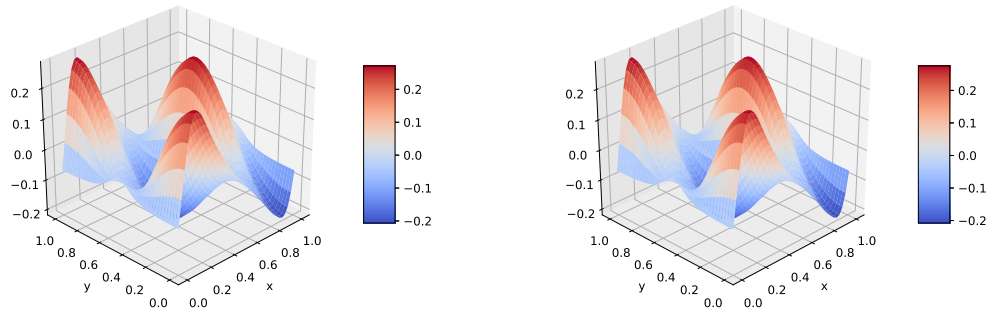
To compute the reference solution, we partition the physical domain $[0, 1]^2$ into $(N_h + 1) \times (N_h + 1)$ grids with mesh size $h = \frac{1}{N_h}$. Similarly, we choose time step $\Delta t = \frac{1}{N_t}$ in discretizing the time domain. As such, $T \times N_t + 1$ snapshots will be generated. In our numerical test, we set $N_h = 80$, $T = 1.0$, and $N_t = 1000$. By applying the algorithm we have discussed in the Section 3.2, we are able to construct a set of POD basis, denoted by $S = \{\psi_1, \dots, \psi_r\}$, $r \leq \min\{(N_h + 1) \times (N_h + 1), T \times N_t + 1\}$. In practice, we determine the number of the POD basis r to be the smallest integer such that $\frac{\sum_{j=r+1}^{N_{snap}} \lambda_j}{\sum_{j=1}^{N_{snap}} \lambda_j} \leq e_{POD}$, where λ_j 's are the eigenvalues of the covariance matrix of the solution snapshots and N_{snap} is the number of solution snapshots, and the constant e_{POD} is chosen to be 0.001 in our numerical experiments. Usually, N_{snap} is assumed to be much smaller than the degree of freedom in the physical space discretization. We choose the inner product in H_1 norm in computing the POD basis.

With the POD basis, we apply the backward Euler and POD-based Galerkin method to compute Eq.(42) with $d = 0.1$. We compare the mean-free POD solution with the mean-free finite difference solution at $T = 1.0s$. Fig.2 shows that the POD solution agrees well with the reference solution. Moreover, based on the mean-free POD solution, we are able to get the numerical solution of the G-equation according to Eq.(23). In Fig.3, we show the recovered solution using our POD method and the reference solution. We can see the good performance of the POD method.

We continue our experiment by computing Eq.(42) with distinct choices of d from 0.01 to 0.1. We compare the error between the POD method and the reference method in computing both the mean-free component of the solution and the recovered solution. Table 1 shows the relative error between these results with different choices of d . We can see the good performance of the POD method and the relative error is much smaller if we add the means back.

In Fig.4 and Fig.5, we show the comparison between the recovered solutions obtained using the POD method and the reference solutions for $d = 0.05$ and $d = 0.01$, respectively. Again, we find that the POD method performs well for all the numerical experiments. In addition, we find that some sharp layers appear in the solution as d decreases. However, our POD basis can capture those layered structures and give accurate numerical results. We also find that the mean-free POD solution agrees well with the mean-free part of the reference solution for different diffusive number d (not shown here).

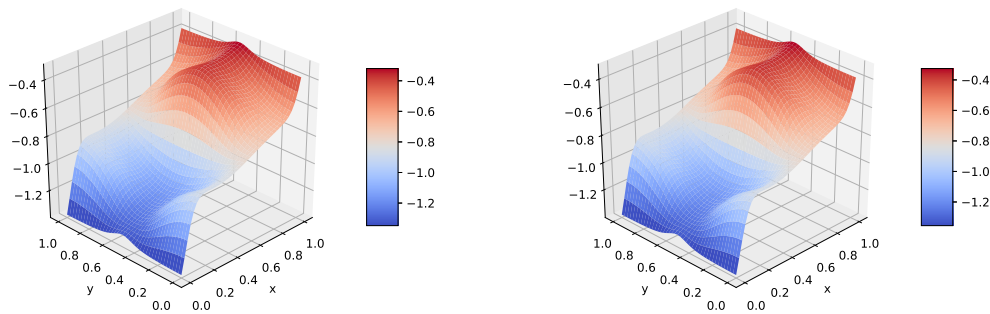
These results show that POD method can capture the low-dimensional structures in the viscous G-equations and provide an efficient model reduction method to approximate the solutions.



(a) Reference solution.

(b) POD solution.

Figure 2: Mean-free component of the solution at $T = 1$ with $d = 0.1$.



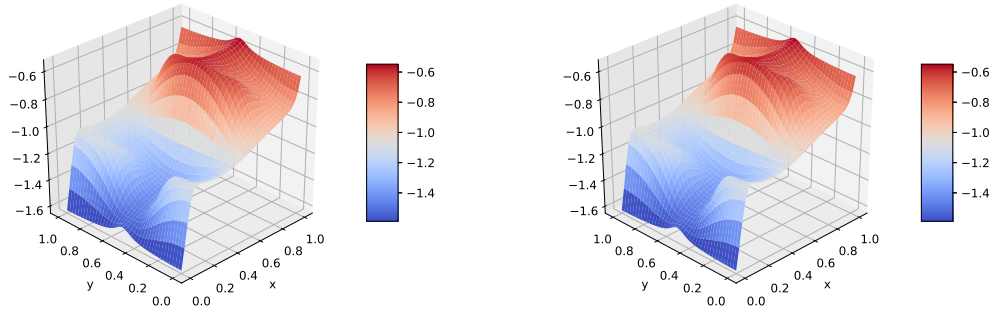
(a) Reference solution.

(b) POD solution.

Figure 3: Solution of the viscous G-equation at $T = 1$ with $d = 0.1$.

d	0.01	0.02	0.03	0.04	0.05
Mean-free component	0.038844	0.069712	0.025673	0.021257	0.017649
Full solution	0.020316	0.026285	0.005110	0.003020	0.003349
d	0.06	0.07	0.08	0.09	0.1
Mean-free component	0.016216	0.014977	0.014998	0.013786	0.013793
Full solution	0.004840	0.004997	0.005115	0.007431	0.007085

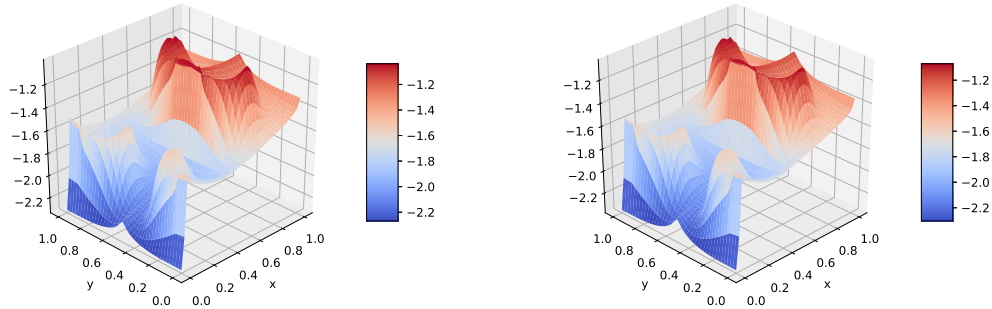
Table 1: The relative errors between POD solution and reference solution.



(a) Reference solution.

(b) POD solution.

Figure 4: Solution of the viscous G-equation at $T = 1$ with $d = 0.05$.



(a) Reference solution.

(b) POD solution.

Figure 5: Solution of the viscous G-equation at $T = 1$ with $d = 0.01$.

5.2. Test of the POD basis for longer time computations

In this numerical experiment, we shall first solve the viscous G-equation (42) from time $t = 0$ to $t = 1$ using the reference numerical scheme to construct POD basis. Then, we recompute the viscous G-equation (42) on a longer time period using the POD basis.

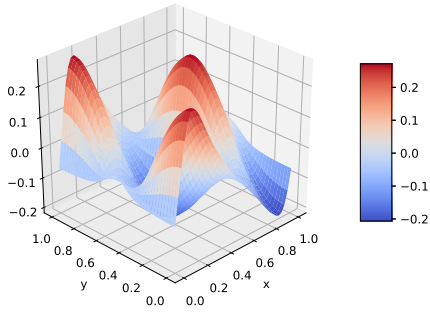
We first compute the viscous G-equation with the diffusive number $d = 0.1$. Fig.6 shows that the mean-free component of the POD solution agrees well with the mean-free component of the reference solution. In addition, Fig.7 shows that the recovered POD solution to the G-equation approximates well with the reference solution. We find that the profiles in Fig.2 and Fig.6, i.e., the mean-free components of the solution are almost the same. Moreover, the profile in Fig.7 is a downward shift of the profile in Fig.3 by 1.4 units. These interesting results show that POD method allows us to compute the stationary solution to the G-equation. In this numerical experiment, the POD method has six basis functions.

We repeat the numerical experiment for different choices of the diffusive number d from 0.1 to 0.01 and compare the error between the POD method and the reference method. Table 2 shows the relative error between these results with different choices of d . We can see the good performance of the POD method and the relative error is much smaller if we add the means back.

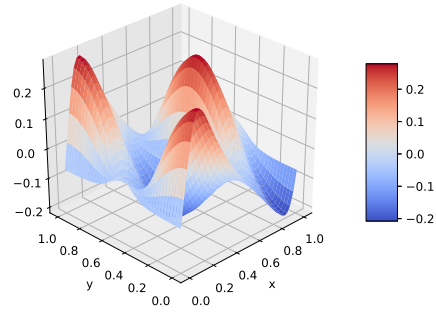
In Fig.8 and Fig.9, we show the comparison between the recovered solutions obtained using the POD method and the reference solutions for $d = 0.05$ and $d = 0.01$, respectively. Again, we find that the POD method performs well for these numerical experiments. Moreover, the profiles in Figs.8 and 9 are downward shifts of the profiles in Figs.4 and 5, respectively. The smaller the d is, the bigger shift will be observed.

5.3. Test of the POD basis for different parameters

We shall investigate the robustness of the POD basis. Specifically, we build the POD basis from the solution snapshots of the viscous G-equation with the diffusivity d_0 . Then,

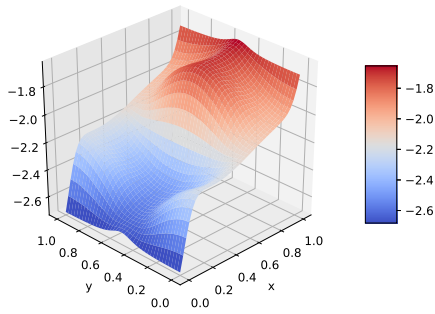


(a) Reference solution.

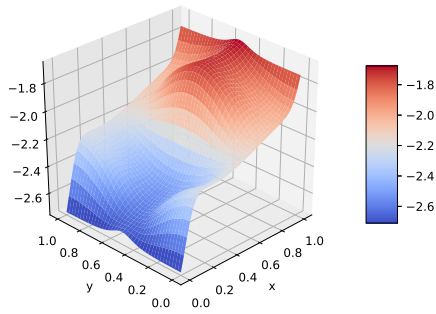


(b) POD solution.

Figure 6: Mean-free component of the solution at $T = 2$ with $d = 0.1$.

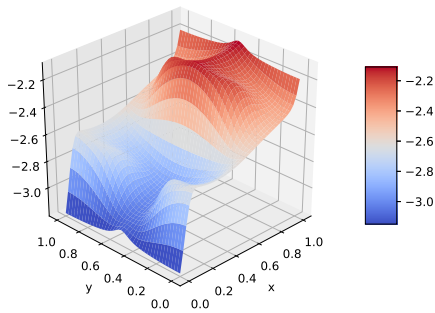


(a) Reference solution.

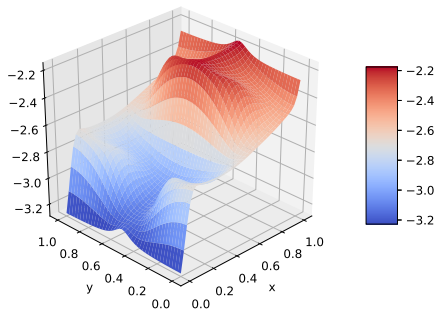


(b) POD solution.

Figure 7: Solution of the viscous G-equation at $T = 2$ with $d = 0.1$.

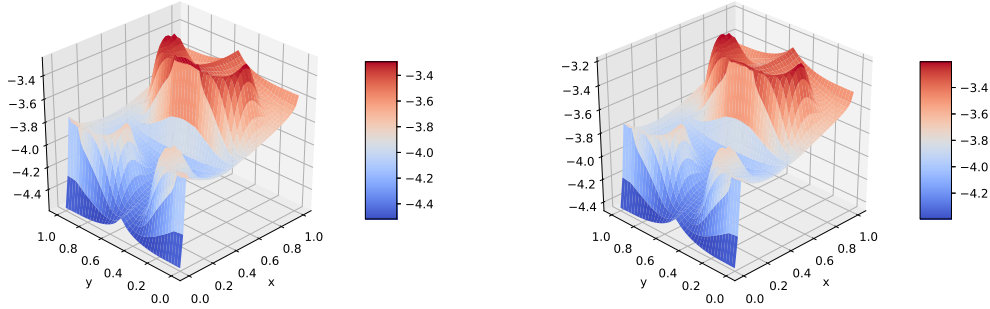


(a) Reference solution



(b) POD solution.

Figure 8: Solution of the viscous G-equation at $T = 2$ with $d = 0.05$.



(a) Reference solution.

(b) POD solution.

Figure 9: Solution of the viscous G-equation at $T = 2$ with $d = 0.01$.

d	0.01	0.02	0.03	0.04	0.05
Rela. error, Mean-free	0.082762	0.042995	0.029778	0.047371	0.042206
Rela. error, Recovered	0.028087	0.020967	0.019781	0.033270	0.026356
d	0.06	0.07	0.08	0.09	0.1
Rela. error, Mean-free	0.038563	0.03471	0.031951	0.029692	0.027939
Rela. error, Recovered	0.020541	0.016758	0.013963	0.012019	0.010648

Table 2: The relative errors between POD solution and reference solution at $T = 2$.

we use the pre-computed POD basis to compute solutions of the viscous G-equation with different d .

In our numerical experiment, we solve the viscous G-equation from $t = 0$ to $t = 1$ with $d_0 = 0.05$ from to build the POD basis. In Table 3, we show the relative errors between the POD solutions and the reference solutions to the viscous G-equation with different d . One can find that POD basis provides good approximations to the solution of the viscous G-equation when d is chosen from $d = 0.01$ to $d = 0.1$. The closer d is close to d_0 , the smaller the error will be. We also observe that POD solutions agree well with the reference solutions to the viscous G-equation with different d (not shown here). We emphasize that the pre-computed POD basis can be used to compute different solutions is of great importance for practical computations.

diffusive number d	0.01	0.02	0.02	0.04	0.05
Rela. error, Recovered	0.056233	0.030934	0.014142	0.008826	0.014398
diffusive number d	0.06	0.07	0.08	0.09	0.1
Rela. error, Recovered	0.018682	0.022199	0.024353	0.025569	0.025963

Table 3: The relative errors between POD solutions and reference solutions.

5.4. Compute the turbulent flame speed

Since the POD basis is very efficient to approximate the solution of the viscous G-equation, we shall apply the newly developed method to compute the turbulent flame speed S_T , which is defined in the Eq.(10). In this experiment, we shall compare the numerical results of the turbulent flame speed obtained using our POD method and the reference method. First of all, for each parameter d we compute the solution snapshots from $t = 0$ to $t = 1$ to construct the POD basis. Then, with the POD basis we solve the viscous G-equation to obtain the solution and the burned area $\mathcal{A}(t)$. Finally, we show the ratio of the $\mathcal{A}(t)$ over time t in Fig.10. These results indicate that the POD basis can be used for long time computation of the viscous G-equation, which allows us to efficiently compute the turbulent flame speed.

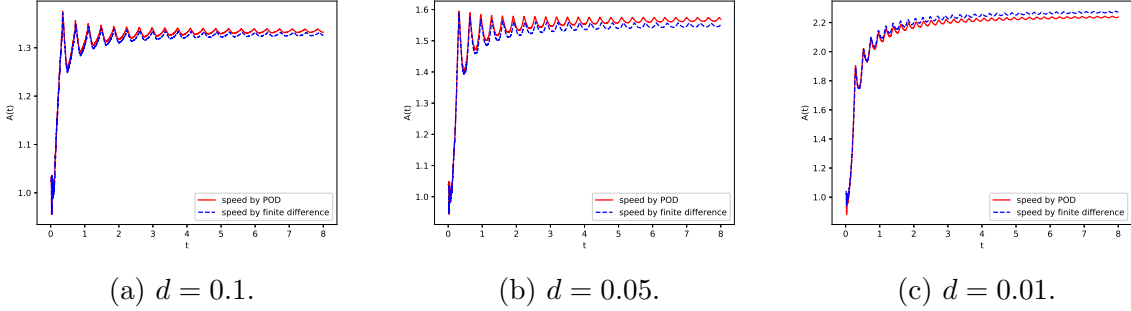


Figure 10: Numerical results of the turbulent flame speed obtained using different methods.

5.5. Comparison of the computational time

In Table 4 we compare the CPU time of two methods when solving the viscous G-equation from time $t = 0$ to $t = 1$ with different d . We find that the CPU time of the POD method slightly increases when d decreases. This is due to the fact that we are using more POD basis for small d in order to achieve the same POD truncation error rate $e_{POD} = 0.1\%$. In general, the computational cost of the POD method is far less than the finite difference method. The unit of the computational time is second.

d	0.01	0.02	0.03	0.04	0.05
POD method	1.438894	1.296282	0.910010	0.945209	0.9290220
Reference method	480.6434	474.2021	483.5336	482.6826	480.4273
d	0.06	0.07	0.08	0.09	0.1
POD method	0.873965	0.940874	0.906758	0.657222	0.786591
Reference method	488.6499	476.8122	487.3498	483.3396	476.7582

Table 4: CPU time of two methods in solving the viscous G-equation from $t = 0$ to 1 with different d .

5.6. Test of the POD basis for a time-periodic fluid velocity

Finally, we consider one parameter family of time-dependent periodic cellular flows

$$\mathbf{V}(\mathbf{x}, t) = (V_1, V_2) = (\cos(2\pi y) + \theta \cos(t) \sin(2\pi y), \cos(2\pi x) + \theta \cos(t) \sin(2\pi x)). \quad (44)$$

The first term of the velocity field $(\cos(2\pi y), \cos(2\pi x))$ is a steady cellular flow, but the second term of the velocity field $\theta \cos(t)(\sin(2\pi y), \sin(2\pi x))$ is a time-periodic perturbation that introduces an increasing amount of disorder in the flow trajectories as θ increases. Again, we compare the numerical results of the turbulent flame speed obtained using our POD method and the reference method.

In Fig.11, we show the ratio of $\mathcal{A}(t)$ over time t with $\theta = 0.05$ and different d . The relative errors for the burning speed are basically negligible. These results show that the POD basis can be used to compute the viscous G-equation with time-periodic cellular flows. Compared with the results in Fig.10, we find that the turbulent flame speed in Fig.11 has different patterns, which is caused by the mixing and chaotic features of the fluid velocity (44).

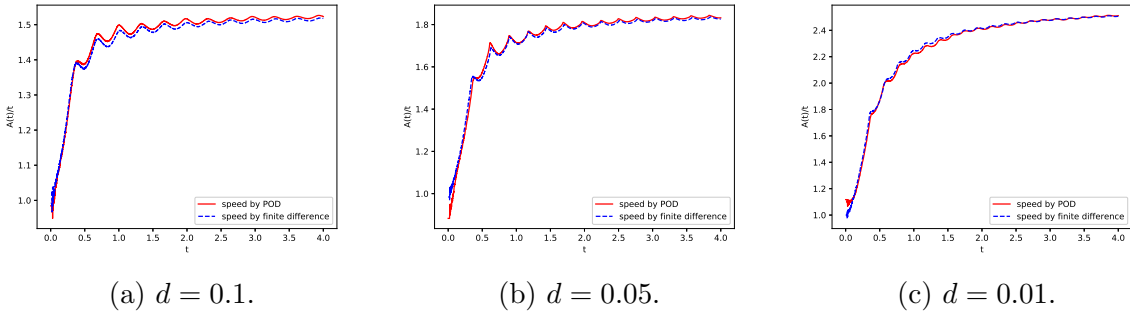


Figure 11: Numerical results of the turbulent flame speed obtained using different methods.

As θ increases, the flow trajectories are more and more mixing and chaotic, which gradually deteriorates the accuracy of the POD method. In Fig.11, we show the ratio of $\mathcal{A}(t)$ over time t with $\theta = 1.0$ and $d = 0.1$. The relative errors for the burning speed are about 2%, which is good enough in the engineering applications. We should point out that when the diffusion parameter d becomes small and θ becomes large, the effective dimension of the G-equation increases fast, which brings difficulty to the POD method. The POD basis obtained by minimizing the projection error, e.g. (20) may not be able to capture the dynamics of the viscous G-equation with time-periodic chaotic flows. One needs other techniques to construct a set of reduced order basis, which will be our subsequent research.

6. Conclusion

We have proposed an efficient model reduction method for solving viscous G-equations, which have been very popular field models in combustion and physics literature for studying turbulent flame propagation. We constructed the POD basis based on learning the

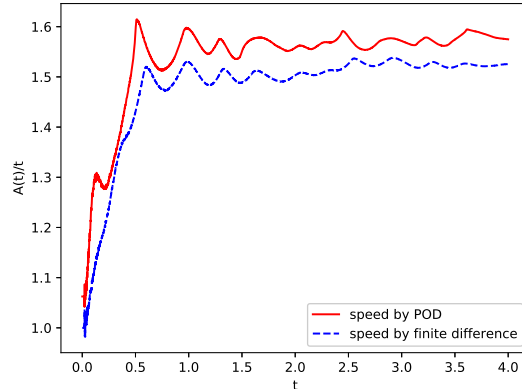


Figure 12: Illustration of local interface velocities in the G-equation and a flame front

solution information from the snapshots. Then, we applied the Galerkin project method to solve the viscous G-equations by using the POD basis. We provided rigorous error analysis for our numerical methods based on a decomposition strategy, where we decomposed the solution into a mean part and a mean-free part. We shown through numerical experiments that our methods can accurately compute the various G-equations with significant computational savings. In addition, we found that the POD basis allows us to compute long-time solution of the various G-equations. Thus, we can evaluated the corresponding turbulent flame speeds in cellular flows. In our future work, we plan to study turbulent flame speeds of G-equations in three dimensional spatially or spatiotemporally periodic vortical flows.

7. Appendix

7.1. A reference method to solve G equation

We first apply the finite difference scheme proposed in [7] to solve the viscous G-equation from time 0 to T seconds on the domain $D = [0, 1] \times [0, 1]$ to get the snapshots. Generally speaking, we employ the Hamilton-Jacobi weighted essentially nonoscillatory (HJ WENO) scheme and the total variation diminishing Runge-Kutta (TVD RK) scheme in higher order spatial and time discretization respectively; see [11, 4, 5, 10] for more details of these schemes.

For small d , the viscous G-equation is convection dominated and it should be treated like a hyperbolic equation. The forward Euler time discretization is given by

$$\frac{G^{n+1} - G^n}{\Delta t} + H^n(G_x^-, G_x^+, G_y^-, G_y^+) - dS_l \Delta G^n = 0 \quad (45)$$

where G_i^- and G_i^+ denote the left and right discretization of G_i in the WENO5 scheme [5]. H is a consistent and monotone numerical Hamiltonian. Here we treat the velocity

term and the normal velocity term separately:

$$H(G_x^-, G_x^+, G_y^-, G_y^+) = V_1 G_x^{vel} + V_2 G_y^{vel} + S_l \sqrt{(G_x^{nor})^2 + (G_y^{nor})^2} \quad (46)$$

where the upwinding scheme and the Godunov scheme are applied for the velocity term and the normal velocity term respectively [10].

$$G_x^{vel} = \begin{cases} G_x^- & \text{if } V_1 > 0 \\ G_x^+ & \text{if } V_1 < 0 \end{cases} \quad (47)$$

$$G_y^{vel} = \begin{cases} G_y^- & \text{if } V_2 > 0 \\ G_y^+ & \text{if } V_2 < 0 \end{cases} \quad (48)$$

$$(G_x^{nor})^2 = \begin{cases} (G_x^-)^2 & \text{if } V_1 > S_l \\ \max(\max(G_x^-, 0)^2, \min(G_x^+, 0)^2) & \text{if } |V_1| \leq S_l \\ (G_x^+)^2 & \text{if } V_1 < -S_l \end{cases} \quad (49)$$

$$(G_y^{nor})^2 = \begin{cases} (G_y^-)^2 & \text{if } V_2 > S_l \\ \max(\max(G_y^-, 0)^2, \min(G_y^+, 0)^2) & \text{if } |V_2| \leq S_l \\ (G_y^+)^2 & \text{if } V_2 < -S_l \end{cases} \quad (50)$$

For the diffusion term, we apply the central difference. For the time discretization, we apply the RK3 scheme [4]. The CFL condition in this case is

$$\Delta t \left(\frac{S_l + |V_1|}{\Delta x} + \frac{S_l + |V_2|}{\Delta y} \right) < 1 \quad (51)$$

When d is large, the time step size for the forward Euler scheme is very small ($\Delta t = O((\Delta x)^2 + (\Delta y)^2)$). To alleviate the stringent time step restriction, we introduce the following semi-implicit scheme:

$$\frac{G^{n+1} - G^n}{dt} + \mathbf{V} \cdot \nabla G^{n+1} + S_l |\nabla G^n| = d S_l \Delta G^{n+1} \quad (52)$$

where the convection and diffusion terms are discretized by the central difference, and the normal direction term is discretized by the Godunov and WENO5 scheme. In this case, the CFL condition is

$$\Delta t \left(\frac{S_l}{\Delta x} + \frac{S_l}{\Delta y} \right) < 1 \quad (53)$$

7.2. Model reduction using the POD method

Let X be a Hilbert space equipped with the inner product $\langle \cdot, \cdot \rangle_X$ and $u(\cdot, t) \in X$, $t \in [0, T]$ be the solution of a dynamic system. In practice, we approximate the space X with a linear finite dimensional space V with $\dim(V) = N_{dof}$, where N_{dof} represents the degree of freedom of the solution space and N_{dof} can be extremely large for high-dimensional

problem (consider the finite element method and finite difference method as examples). Given a set of snapshot of solutions, a linear space S can be spanned, denoted as $S = \text{span}\{u(\cdot, t_1), u(\cdot, t_2), \dots, u(\cdot, t_m)\}$, where $t_1, \dots, t_m \in [0, T]$ are different time instances and m is the number of the solution snapshots.

The POD method aims to build a set of low-dimensional basis $\{\psi_1(\cdot), \psi_2(\cdot), \dots, \psi_r(\cdot)\}$ with $r \leq \min(m, N_{dof})$ that optimally approximates the input solution snapshots. More specifically, the POD seeks a solution for the following optimization problem:

$$\min_{\psi_1, \dots, \psi_r \in X} \frac{1}{m} \sum_{i=1}^m \|u(\cdot, t_i) - \sum_{j=1}^r \langle u(\cdot, t_i), \psi_j(\cdot) \rangle_X \psi_j(\cdot)\|_X^2, \quad \text{s.t. } \langle \psi_i, \psi_j \rangle_X = \delta_{ij} \quad (54)$$

In order to solve Eq.(54), we consider the eigenvalue problem

$$Kv = \lambda v$$

where $K \in \mathbb{R}^{m \times m}$ and $K_{ij} = \frac{1}{m} \langle u(\cdot, t_i), u(\cdot, t_j) \rangle_X$ is the snapshot correlation matrix. Let $v_k, k = 1, \dots, m$ be the eigenvectors and $\lambda_1 \geq \lambda_2 \geq \dots \geq \lambda_m > 0$ be the positive eigenvalues. It has been shown in [15] that the solution of 54 is given by

$$\psi_k(\cdot) = \frac{1}{\sqrt{\lambda_k}} \sum_{j=1}^m (v_k)_j u(\cdot, t_j), \quad 1 \leq k \leq r \quad (55)$$

It can also be shown that the following error formula holds

$$\frac{1}{m} \sum_{i=1}^m \|u(\cdot, t_i) - \sum_{j=1}^r \langle u(\cdot, t_i), \psi_j(\cdot) \rangle_X \psi_j(\cdot)\|_X^2 = \sum_{j=r+1}^m \lambda_j \quad (56)$$

We use the notation S^r to denote the span of $\{\psi_1(\cdot), \psi_2(\cdot), \dots, \psi_r(\cdot)\}$.

Acknowledgement

The research of J. Xin is partially supported by NSF grants DMS-1211179 and DMS-1522383. The research of Z. Zhang is supported by Hong Kong RGC grants (Projects 27300616, 17300817, and 17300318), National Natural Science Foundation of China (Project 11601457), Seed Funding Programme for Basic Research (HKU), and an RAE Improvement Fund from the Faculty of Science (HKU).

References

- [1] P. Benner, S. Gugercin, and K. Willcox. A survey of projection-based model reduction methods for parametric dynamical systems. *SIAM review*, 57(4):483–531, 2015.
- [2] J. Borggaard, T. Iliescu, and Z. Wang. Artificial viscosity proper orthogonal decomposition. *Mathematical and Computer Modelling*, 53(1-2):269–279, 2011.

- [3] P. Embid, A. Majda, and P. Souganidis. Comparison of turbulent flame speeds from complete averaging and the G-equation. *Physics of Fluids*, 7(8):2052–2060, 1995.
- [4] S. Gottlieb and C. Shu. Total variation diminishing runge-kutta schemes. *Mathematics of computation of the American Mathematical Society*, 67(221):73–85, 1998.
- [5] G. Jiang and D. Peng. Weighted eno schemes for hamilton–jacobi equations. *SIAM Journal on Scientific computing*, 21(6):2126–2143, 2000.
- [6] K. Kunisch and S. Volkwein. Galerkin proper orthogonal decomposition methods for parabolic problems. *Numerische mathematik*, 90(1):117–148, 2001.
- [7] Y. Liu, J. Xin, and Y. Yu. A numerical study of turbulent flame speeds of curvature and strain g-equations in cellular flows. *Physica D: Nonlinear Phenomena*, 243(1):20–31, 2013.
- [8] G. Markstein. *Nonsteady flame propagation*. Pergamon Press, Oxford, 1964.
- [9] B. Matkowsky and G. Sivashinsky. An asymptotic derivation of two models in flame theory associated with the constant density approximation. *SIAM Journal on Applied Mathematics*, 37(3):686–699, 1979.
- [10] S. Osher and R. Fedkiw. *Level set methods and dynamic implicit surfaces*, volume 153. Springer Science & Business Media, 2006.
- [11] S. Osher and J. Sethian. Fronts propagating with curvature-dependent speed: algorithms based on Hamilton-Jacobi formulations. *Journal of computational physics*, 79(1):12–49, 1988.
- [12] N. Peters. *Turbulent combustion*. Cambridge university press, 2000.
- [13] C. Shu and S. Osher. Efficient implementation of essentially non-oscillatory shock-capturing schemes. *Journal of computational physics*, 77(2):439–471, 1988.
- [14] V. Thomée. *Galerkin finite element methods for parabolic problems*, volume 1054. Springer, 1984.
- [15] S. Volkwein. Proper orthogonal decomposition: Theory and reduced-order modelling. *Lecture Notes, University of Konstanz*, 4(4), 2013.
- [16] J. Xin. *An introduction to fronts in random media*, volume 5. Springer Science & Business Media, 2009.